Electrochimica Acta 105 (2013) 514–523

Contents lists available at SciVerse ScienceDirect

Electrochimica Acta

journal homepage: www.elsevier.com/locate/electacta

Characterization of electrochemical properties of a micro–nanochannel integrated system using computational impedance spectroscopy (CIS)

Vishal V.R. Nandigana, N.R. Aluru*

Department of Mechanical Science and Engineering, Beckman Institute for Advanced Science and Technology, University of Illinois at Urbana-Champaign, Urbana, IL 61801, USA

ARTICLE INFO

Article history:
Received 5 March 2013
Received in revised form 2 May 2013
Accepted 8 May 2013
Available online 16 May 2013

Keywords:
Micro–nanochannel
Impedance spectroscopy
Area-averaged model
Concentration polarization
Overlimiting current

ABSTRACT

The integration of a microchannel with an ion-selective nanochannel exhibits nonlinear current–voltage characteristics owing to the concentration polarization effects. In this paper, an efficient computational impedance spectroscopic technique (CIS) is developed using an area averaged multi-ion transport model (AAM). Using this technique, we investigate the ion transport dynamics in the Ohmic and non-Ohmic regions. Under no external *DC* bias and in the Ohmic regime, we observe two distinct arcs. The low frequency diffusional arc characterizes the diffusion-transport and the electrical double layer (EDL) charging effects at the interface of the micro–nanochannel, while the high frequency geometric arc characterizes the electric migration and displacement current effects inside the nanochannel and in the microchannel. Further, we observe an anomalous inductive arc at low frequencies ($fL_m^2/D \leq 1$), in the overlimiting regime. This arc is primarily attributed to the phase effects between the first harmonic contribution of the total ionic concentration and the electric field in the induced space charge region. The microscopic diffusion boundary layer (DBL) lengths observed in the microchannel are also efficiently characterized from the impedance spectrum. Equivalent circuit models are designed to interpret the impedance response.

1. Introduction

Nanofluidic devices are being fabricated at a rapid rate in recent years [1], as they are attracting tremendous interest from diverse fields including chemistry, physics, engineering and biological life sciences [2–5]. This stems from the fact that a nanopore can be used for a variety of applications, including single molecule/particle sensing [6,7], DNA sequencing [8–11], preconcentration of analytes using electric field focusing [12] and water desalination [13]. In all these applications, the nanochannel is typically integrated with a microchannel on either side and a potential difference is applied between the ends of the microchannel [12,14–16]. The microchannel influences the transport inside the ion-selective nanochannel under higher electric fields due to concentration polarization effects [17–20]. The micro–nanochannel integrated electrochemical system (MNECS) displays current rectification behavior, resulting in three different regimes, namely, Ohmic, finite differential limiting resistance and overlimiting regimes [21–23].

Conductivity measurements obtained using *DC* voltammetry are useful in providing evidence for the interfacial double layer effects near the micro–nanochannel, and the electrostatic interactions near the nanochannel surface. However, fundamental knowledge regarding the phase sensitive capacitive and inductive effects in these systems is inaccessible through *DC* measurements. Impedance spectroscopy technique, which measures the complex impedance response of the system as a function of frequency [24] is currently being used to understand the dynamics in ion-selective systems [4,25–30]. As different frequency ranges can be selected, the phase sensitive information can be experimentally measured. Though there has been some recent experimental progress to understand the electrochemical transport in nanopore geometry, there is inadequate theoretical/computational development to understand the impedance response of micro–nanochannel integrated systems. This is due to the computational challenges encountered in modeling the multi-domain and multi-phenomenon system. Hence an equivalent circuit modeling approach is preferred to fit the experimental observations. However, it is important to note that the same data can be modeled using different equivalent circuits which may not depict the exact physical nature of the problem.

In this paper, we develop an area-averaged multi-ion transport model (AAM), considering the entire micro–nanochannel system. A computational impedance spectroscopic technique (CIS)

* Corresponding author. Tel.: +1 217 333 1180; fax: +1 217 244 4333.
E-mail addresses: aluru@illinois.edu, aluru@uiuc.edu (N.R. Aluru).
URL: http://www.illinois.edu/~aluru (N.R. Aluru).

0013-4686/$ – see front matter © 2013 Elsevier Ltd. All rights reserved.
http://dx.doi.org/10.1016/j.electacta.2013.05.011

is developed to characterize the electrochemical properties of the system. In this method, we apply a small amplitude periodic electric potential disturbance (*AC*) over a wide range of frequency spectrum along with a constant electric potential (*DC*). The technique is used to study the ion-transport dynamics in the Ohmic and non-Ohmic regimes. The model considers the effect of displacement current along with the conduction current contribution due to diffusion and electric migration processes.

In the Ohmic region, we observe multiple arcs in the impedance spectrum, which is attributed to the diffusion-transport near the micro–nanochannel interface, and the transport effects inside the nanochannel. In the limiting resistance region (LRR), an additional resistance–capacitance (RC) arc is observed. This is primarily due to the space charges induced near the micro–nanochannel depletion interface. Further, an anomalous inductive arc is observed in the overlimiting regime. The origin of this arc is discussed. Using the impedance spectra, we also highlight the important time scales at which negative and positive *AC* rectification effects are observed in the system.

2. Theory

2.1. Area-averaged multi-ion transport model (AAM)

In equilibrium and under the Ohmic regime, a typical micro–nanochannel integrated system (see Fig. 1(a)) can be divided into 5 different regions including the ion-selective nanochannel. At both the interfaces of the micro–nanochannel, we observe a thin electrical double layer (EDL) region. An electroneutral enrichment and depletion diffusion boundary layers (DBL) are observed adjacent to the EDL region. The DBL region extends until the ends of the microchannel, where the concentration of the ionic solution is the bulk ionic concentration (c_0). The EDL and DBL regions are formed outside the nanochannel owing to the concentration polarization effects [18]. A schematic representation of all these regions is shown in Fig. 1(a). Under the application of high electric fields, the integrated system experiences nonlinear current characteristics. Using a 2-D continuum based nonlinear ion-transport model, the transition from the limiting resistance region to a

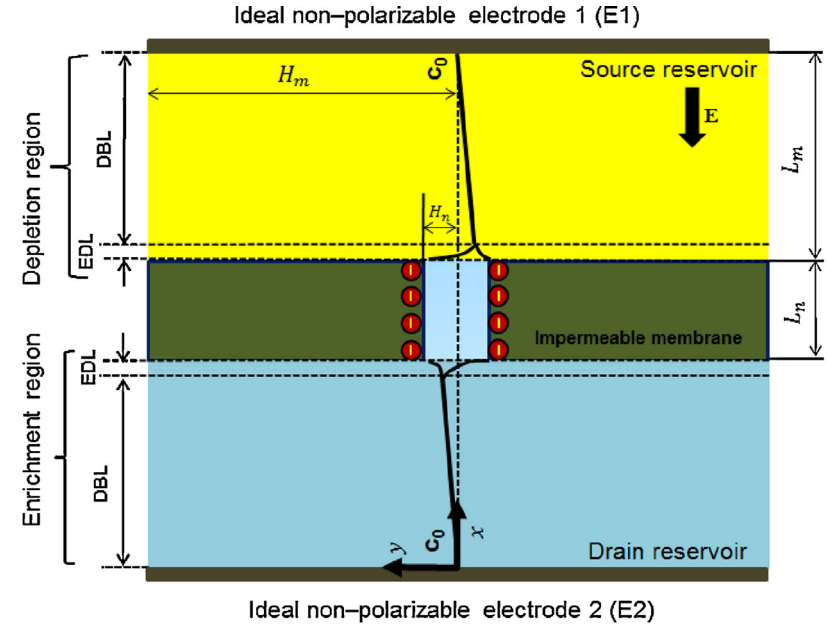

(a)

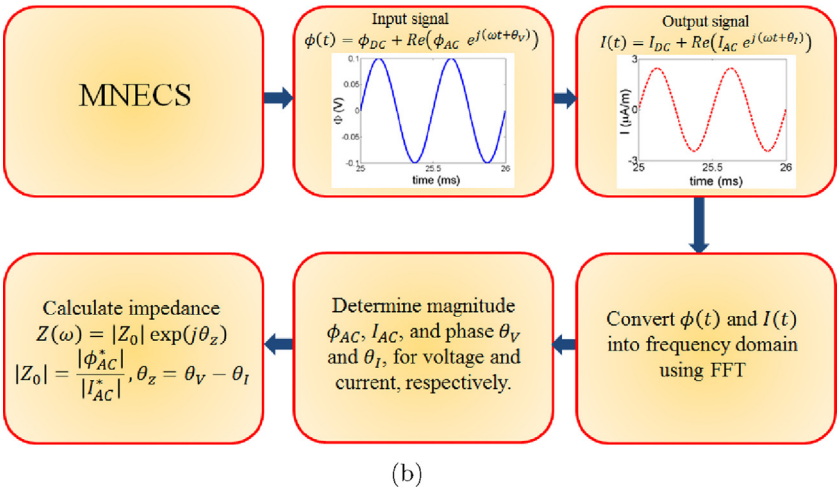

(b)

Fig. 1. (a) A canonical hybrid micro–nanochannel integrated electrochemical system (MNECS). The bold line displays the ionic concentration distribution indicating the enrichment and depletion electroneutral diffusion boundary layer (DBL) under Ohmic regime. A thin quasi-equilibrium EDL developed on both sides near the micro–nanochannel interface is also shown. c_0 refers to the bulk ionic concentration at the ends of the microchannel. (b) Flow chart to characterize the electrochemical properties of MNECS.

constant conductivity overlimiting behavior was attributed to the redistribution of the charges near the micro–nanochannel depletion interface [17]. The fluidic nonlinearity was found to play a minimal role during this transition. However, the 2-D model offers computational challenges to study the impedance response of MNECS over a wide range of frequency spectrum. Hence, we propose a computationally efficient area averaged multi-ion transport model, considering the entire micro–nanochannel system. We neglect the fluidic effects in the model due to the aforementioned reasons. A systematic reduction of the 2-D nonlinear model into a dimensionless area-averaged model and the necessary boundary conditions are discussed in the supporting information.

From the governing equations, we obtain an important non-dimensional number, $\beta = \lambda_D/L_m$. It characterizes the effect of the electrolyte concentration in the system as the Debye length ($\lambda_D = \sqrt{\epsilon_0\epsilon_r RT/2F^2z^2c_0}$) determines the thickness of the EDL. L_m is length of the microchannel. ϵ_0 is the permittivity of free space and ϵ_r is the relative permittivity of the medium. The constants F, R, and T represent Faraday's constant, ideal gas constant and absolute thermodynamic temperature, respectively. In this work, a symmetric monovalent electrolyte ($z_+ = -z_- = z$) like KCl is considered and we normalize the diffusion coefficient of each ionic species with the characteristic diffusion coefficient, $D = 2\times10^{-9}\,m^2/s$. New solvers for the area-averaged transport model are developed and implemented using the finite volume method in OpenFOAM (Open Field Operation and Manipulation) version 1.6 [31]. The model is validated with the 2-D model developed in our earlier work. The details are presented in the supporting information.

2.2. Computational impedance spectroscopy (CIS)

In order to study the ion transport dynamics in MNECS, the applied electric potential ($\phi(t)$) and the output current per unit width ($I(t)$) are expressed in complex form as;

$$\phi(t) = \phi_{DC} + \phi_{AC}sin(\omega t) = \phi_{DC} + Re(\phi_{AC}e^{j(\omega t+\theta_V)}) \quad (1)$$

$$I(t) = I_{DC} + Re(I_{AC}e^{j(\omega t+\theta_I)}) \quad (2)$$

where ϕ_{DC} and I_{DC} are the DC component of the electric potential and current per unit width, respectively. ϕ_{AC} and I_{AC} represent the amplitude of the perturbed AC electric potential and current per unit width, respectively. ω is the applied angular frequency ($\omega = 2\pi f$, f is the applied frequency) and Re is the operator "real part of". $\theta_V (= 3\pi/2)$ is the fixed phase angle of the applied harmonic electric potential, θ_I represents the phase angle of the perturbing electric current. We would like to point out that the output current per unit width is calculated at the end of the source reservoir. It is then converted into frequency domain using the fast Fourier transform (FFT) algorithm in Matlab [32] to obtain the amplitude and phase information. The details of the algorithm are presented in the supporting information. The complex electrochemical impedance is given by $Z(\omega) = |Z_0|e^{j\theta_z} = Re(Z) + jIm(Z)$. $|Z_0| = |\phi^*_{AC}|/|I^*_{AC}|$ is the magnitude of the normalized electrochemical impedance, considering the normalized perturbed potential, $\phi^*_{AC} = \phi_{AC}Fz/RT$, and the normalized perturbed current per unit width, $I^*_{AC} = I_{AC}/FzDc_0$. $\theta_z = \theta_V - \theta_I$ is the relative phase difference between the applied harmonic electric potential and the perturbing current, and $j = \sqrt{-1}$ is the imaginary unit. Knowing the magnitude and phase of the impedance, we calculate the normalized real $\left(Re(Z) = |Z_0|cos\theta_z\right)$ and the imaginary ($Im(Z) = |Z_0|sin\theta_z$) part of the impedance, respectively. A flow chart to calculate the impedance response of MNECS is shown in Fig. 1(b).

3. Simulation details

The simulated domain consists of a rectangular nanochannel of length $L_n = 5\,\mu m$ and half height $H_n = 15\,nm$ connected to two microchannels of length $L_m = 6\,\mu m$ and half height $H_m = 500\,nm$, on either side of the nanochannel (see Fig. 1(a)). The operating temperature is $T = 300\,K$. The diffusivities of K^+ and Cl^- are $1.96\times10^{-9}\,m^2/s$ and $2.03\times10^{-9}\,m^2/s$, respectively. We assume the dielectric constant of the aqueous solution to be, $\epsilon_r = 80$ [33]. We neglect the changes in the surface chemistry at the walls of the microchannel due to the ionic solution concentration. Hence, we consider zero surface charge density on the microchannel walls, $\sigma_m = 0$. This assumption is justified as the microchannel wall surface has typically little/no influence on the ion-transport, near the micro/nanochannel interface and within the nanochannel. This is due to the fact that the height of the microchannel considered is atleast two orders of magnitude greater than the nanochannel height. In this study, we primarily focus our attention on understanding the EDL effects at the interface, and hence, assume a constant and a homogeneous surface charge density on the walls of the nanochannel, $\sigma_n = -1\,mC/m^2$.

4. Results and discussion

4.1. Impedance characteristics under no DC bias

Fig. 2(a) shows the normalized impedance spectrum in the form of a Nyquist plot (-Imaginary(Z) vs Real(Z)) under no external DC bias. The applied frequency, f, increases from the right to the left of the plot. In this case, we consider a low bulk ionic concentration, $c_0 = 0.1\,mM$ (corresponding to a thick EDL regime, $\beta = 5.1334\times10^{-3}$) and apply a small AC amplitude, $\phi_{AC}Fz/RT = 3.8683$. A frequency range from 5 Hz to 5 MHz is applied to understand the phase sensitive electrochemical properties. The spectrum reveals two distinct arcs. We define the arc in the low frequency regime as the diffusional arc. This is because this arc characterizes the diffusion-transport outside the nanochannel. In the diffusional arc, the Nyquist plot shows a linear behavior at its high frequency edge near the point of coincidence of the two arcs. This linear behavior is in accordance with the classical Warburg type impedance for semi-infinite oscillating diffusion [24]. However, the diffusional arc closes back on the real axis in an arc as the frequency approaches zero. The finite diffusion lengths are attributed to the breakdown of the Warburg impedance [34,35]. The characteristic diffusional arc can be represented by the diffusion (–O–) circuit element or also referred to as the open finite length diffusion circuit element ($Z_D(\omega)$) [36],

$$Z_D(\omega) = R_D\frac{tanh[\sqrt{(j\omega\tau_D)}]}{\sqrt{(j\omega\tau_D)}} \quad , \quad (3)$$

where R_D depicts the interfacial resistance contributed by both the EDLs and the resistance in the enrichment and depletion DBL due to the concentration gradients. $\tau_D = (L^2_{DBL})/D$, is the diffusional relaxation time relating the length of the diffusion boundary layer (L_{DBL}) and the diffusion coefficient of the ions in this layer. It is well known that the imaginary part of the impedance (with the negative sign) for the diffusion O element reaches a maximum when $\omega\tau_D = 2.54$ [37], i.e., at the characteristic frequency given by $f_D = (2.54D)/(2\pi L^2_{DBL})$. From our simulations, Fig. 2(a) shows that this frequency (f_D) is around 20 Hz. Substituting in the aforementioned relation results in the estimation of the length of the electroneutral diffusion boundary layer which is approximately equal to the length of the microchannel. The result is consistent as the system is almost electroneutral through out the microchannel, when there is no external DC bias. We also note that in the

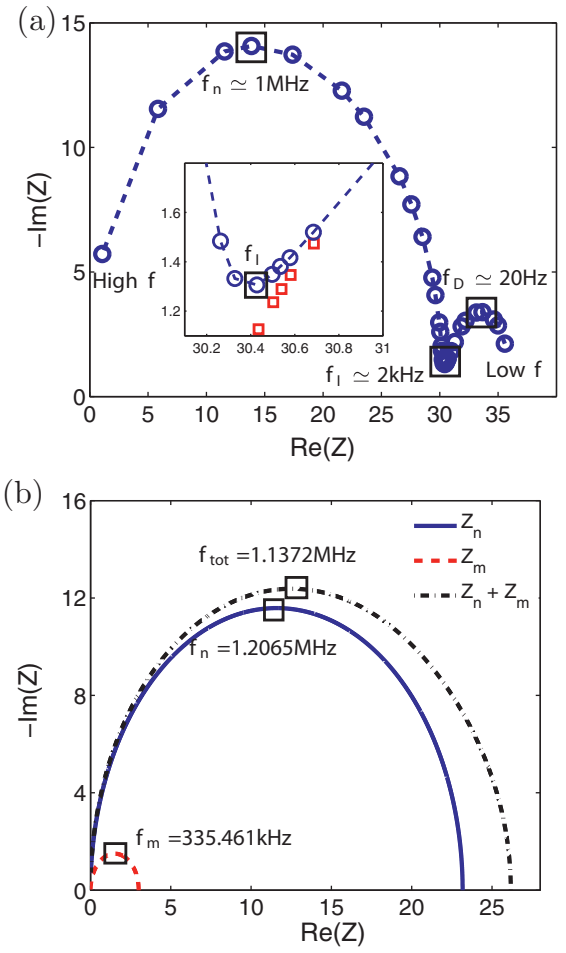

Fig. 2. (a) Impedance spectra (Nyquist plot) for a bulk ionic concentration $c_0 = 0.1$ mM, corresponding to $\beta = 5.1334 \times 10^{-3}$, under no external *DC* bias. The inset of Fig. 2(a) shows a comparison of impedance spectra with (dashed line with symbols) and without (open squares) the displacement current effects, near the characteristic frequency, f_I. (b) Analytical impedance response of a microchannel (dashed line), nanochannel (solid line) and their combined response (dash dot-line).

diffusional arc, when the applied frequency is less than f_D, we do not observe any contribution from the displacement current (as the rate of change of electric displacement field is negligible at such low applied frequencies). Hence, there is no charging of the EDL at these frequencies and it can be assumed to be in equilibrium. However, for $f > f_D$, the inset of Fig. 2(a) shows a higher $-Im(Z)$ when the displacement current is considered compared to the case without considering them. The higher $-Im(Z)$ indicates the charging of the EDL at frequencies beyond f_D. Thus, the impedance response in the EDL and DBL regions due to the combined diffusional and displacement current outside the nanochannel can be represented by considering a diffusion O element in parallel with an EDL capacitor.

In Fig. 2(a) we define the second arc in the high frequency regime as a geometric arc. We observe a distorted hemicircle in this arc. In order to understand this we consider the electromigration processes in both the microchannels and inside the nanochannel. Also, under no external *DC* bias, the system symmetry is still restored. The solution resistance (R_m) (owing to the migration process) and the corresponding capacitance (C_m) (due to the displacement current) in both the microchannels are the same. Hence, the characteristic frequency can be estimated by considering the resistance and capacitance of a single microchannel. Here, we consider the depletion microchannel for the analysis. Further, R_m and C_m are both parallel to each other as they are contributed by two different currents which are additive. Assuming a symmetric monovalent electrolyte, with equal diffusivities ($D_+ = D_- = D$) and neglecting the diffusional and displacement current, we obtain the current per unit width (I) in the $x-$direction inside the microchannel

$$I = -\frac{2F^2 z^2 D H_m}{RT} \frac{d\hat{\phi}}{dx} (\hat{c}_+ + \hat{c}_-) \tag{4}$$

Here$\hat{}$ denotes the area averaged quantity considering the width of the system to be unity. Under no external *DC* bias, neglecting the EDL effects, local electroneutrality is maintained throughout the microchannel, and is equal to the bulk ionic concentration ($\hat{c}_+ = \hat{c}_- = c_0$). Upon integrating Eq. (4) along the length of the source microchannel and substituting the above condition, the solution resistance of the microchannel is $R_m = (RTL_m)/(4F^2 z^2 D H_m c_0)$. The corresponding capacitance of the microchannel is $C_m = 2\epsilon_0 \epsilon_r H_m / L_m$. Using R_m and C_m, the characteristic frequency of the source microchannel is $f_m = 1/(2\pi R_m C_m) = D/(2\pi\lambda_D^2)$. Following the above procedure, the current per unit width inside the nanochannel is $I = -[(2F^2 z^2 D H_n)/(RT)](d\phi/dx)(\hat{c}_{n+} + \hat{c}_{n-})$. Here $\hat{c}_{n+}$ and $\hat{c}_{n-}$ are the counter-ion and co-ion concentrations inside the nanochannel (averaged over the height of the nanochannel). The individual ionic concentrations inside the nanochannel can be approximately calculated using the Donnan equilibrium theory [5] as $\hat{c}_{n\pm} = \pm\bar{c}/2 + \sqrt{(\bar{c}/2)^2 + c_0^2} \cdot \bar{c} = \hat{c}_{n+} - \hat{c}_{n-} = -\sigma_n / FzH_n$, is obtained from the electroneutrality condition inside the nanochannel, considering the nanochannel wall surface charge density effects. Substituting the above expressions and integrating the current per unit width along the length of the nanochannel, the resistance of the nanochannel is given by $R_n = (RTL_n)/(2F^2 z^2 D H_n (\hat{c}_{n+} + \hat{c}_{n-}))$. Knowing the nanochannel capacitance $C_n = 2\epsilon_0 \epsilon_r H_n / L_n$, the characteristic frequency of the nanochannel is $f_n = 1/2\pi R_n C_n = (F^2 z^2 D(\hat{c}_{n+} + \hat{c}_{n-}))/(2\pi RT \epsilon_0 \epsilon_r)$. R_n and C_n are parallel to each other owing to the similar arguments discussed for the microchanne

The impedance $Z(\omega)$ for a simple resistor (R) and capacitor (C) in parallel is $Z(\omega) = \left(1/R + j\omega C\right)^{-1}$. Substituting the aforementioned expressions for R_m, C_m, R_n, C_n, we calculate the individual impedance of the source microchannel (Z_m) and nanochannel (Z_n). Fig. 2(b) shows the impedance response of the source microchannel, nanochannel and the total response ($Z_m + Z_n$) in the form of a normalized Nyquist plot. The total impedance response is obtained by considering Z_m and Z_n in series with each other. We observe that the imaginary part of the nanochannel impedance ($-Im(Z)|_n$) is greater than the source microchannel ($-Im(Z)|_m$). Also, f_m, related to the source microchannel, is smaller compared to the characteristic frequency of the nanochannel (f_n). As the frequency increases beyond f_m, $-Im(Z)|_m$ reduces, and when the applied frequency approaches f_n, the imaginary part of the microchannel impedance is small. Hence, the sum $-(Im(Z)|_m + Im(Z)|_n)$ is approximately equal to $-Im(Z)|_n$. Thus, the frequency related to the maximum of imaginary part of nanochannel + microchannel impedance is approximately closer to f_n. While at low frequencies, close to f_m, the contribution of $-Im(Z)|_m$ in the sum is considerable that results in a deviation from a perfect hemicircle. From the above analysis, we also understand that when $f_n \gg f_m$, there would be two semicircles related separately to the nanochannel and the microchannel. We also observe another characteristic frequency "f_I'' where the diffusional and the geometric arc meet (see Fig. 2(a)). This frequency approximately corresponds to the geometric mean of $f_D (\propto D/L_{DBL}^2)$ and $f_m (\propto D/\lambda_D^2)$, which reveals that f_I is proportional to $D/(\lambda_D L_{DBL})$. When the applied frequency is between f_D and f_I, the charging of the EDL is observed resulting in a higher $-Im(Z)$ compared to the case without considering the displacement current as shown in the inset of Fig. 2(a). This reveals that the EDL capacitance is dominant at frequencies of the order of f_I. Further at frequencies greater than f_I, the capacitance of the nanochannel (C_n) and the microchannel (C_m) dominate compared to the EDL capacitance. From the preceding

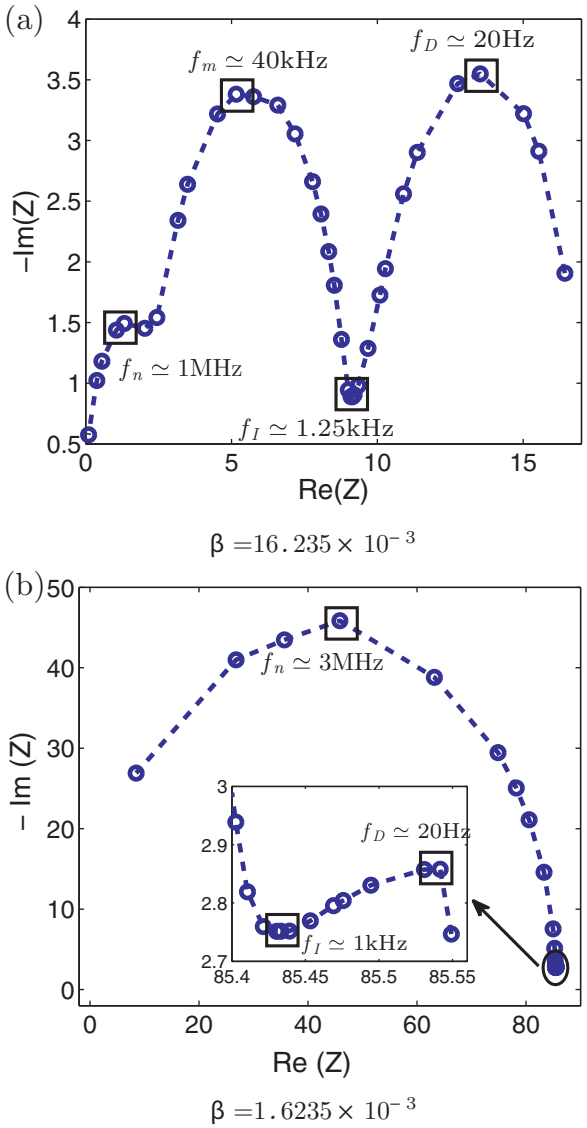

Fig. 3. Impedance spectra (Nyquist plot) for different dimensionless electrolyte concentration (β), under no external *DC* bias. The inset of part figure (b) shows the small diffusional arc in the low frequency regime.

expressions for f_n, f_m and f_I, we observe that these three characteristic frequencies are dependent on the bulk ionic concentration. In order to establish consistency in our hypothesis, we perform computations at different bulk electrolyte concentration, $c_0 = 0.01$ mM (see Fig. 3(a)), and 1 mM (see Fig. 3(b)). This corresponds to $\beta = 16.235 \times 10^{-3}$ and $\beta = 1.6235 \times 10^{-3}$, respectively.

Fig. 3(a) reveals both the characteristic frequencies f_m and f_n in the geometric arc. When the bulk ionic concentration is reduced by an order of magnitude, the resistance of the microchannel (R_m) increases by one order and C_m is independent of the concentration variation. The increase in the microchannel resistance decreases f_m by one order. The approximate analytical values of f_m (= 33.546 kHz) and f_n (= 1.159 MHz) are in close agreement with the numerical simulations. From the earlier discussion, as $f_n \gg f_m$ it is possible to distinguish the two arcs corresponding to the migration processes inside the microchannel and the nanochannel. Further for the bulk concentration considered, the resistance of the microchannel is found to be greater than the nanochannel resistance. This results in a higher impedance of the microchannel arc compared to the nanochannel. Fig. 3(a) shows that the diffusional arc in this case becomes predominant due to the thick electrical double layer

Table 1
Effect of bulk ionic concentration on the impedance spectra corresponding to diffusion and nanochannel characteristic frequencies, $\chi = (Im(Z)\big|_{f_D})/(Im(Z)\big|_{f_n})$

c_0 (mM)	$\beta(\times 10^{-3})$	χ
0.01	16.235	2.3787
0.1	5.1334	0.2408
1	1.6235	0.0623

formed at the interface of the micro–nanochannel. However, the frequency f_D is found to be independent of the electrolyte concentration (consistent with the expression obtained for f_D), while f_m, f_n and f_I were found to vary with the concentration. Similar characteristics are also observed at $\beta = 1.6235 \times 10^{-3}$ as shown in Fig. 3(b). However, we notice that, it is difficult to observe the diffusion arc at this concentration (see inset of Fig. 3(b)). This can be understood from the fact that, at high concentration limit, the electrical double layer at the interface diminishes resulting in a decrease in the resistance R_D.

In order to understand the contribution of diffusion-transport at the micro–nanochannel interface compared to the migration effects inside the nanochannel, for different bulk concentrations, we calculate the ratio of the imaginary part of the impedance corresponding to the diffusional and nanochannel characteristic frequencies ($\chi = (Im(Z)|_{f_D})/(Im(Z)|_{f_n})$). Table 1 shows that at a very low bulk ionic concentration, $\beta = 16.235 \times 10^{-3}$, the diffusion-transport near the interface is nearly 2.4 times dominant compared to the migration effects inside the nanochannel. However, with increase in the ionic concentration, we observe a power law type decrease in χ. The contribution of the diffusion-transport near the interface reduces to 6% compared to the transport effects inside the nanochannel for a high bulk electrolyte concentration, $\beta = 1.6235 \times 10^{-3}$. Fig. 3(b) also shows that the geometric arc is close to a perfect hemicircle. This can be attributed to two reasons. First, the surface charge density on the walls of the nanochannel play a minimal role as the electrostatic interactions near the surface is screened by the excess ions. Second, the resistance and hence the impedance response of the microchannel is minimal due to the large bulk electrolyte concentration.

Additional simulations are performed by varying the microchannel geometry to ensure that the DBL length (obtained from f_D) is characterized efficiently. The results are presented in the supporting information (see Fig. (S2)).

4.2. Effect of DC potential bias

In the above studies, we assumed that the system is not subjected to an external *DC* bias. However, it is equally important to characterize the system under different *DC* bias owing to the nonlinear current characteristics beyond a critical voltage. Fig. 4(a) compares the spectra in the Ohmic-regime ($\phi_{DC}Fz/RT = 3.8684$), with that of the no bias case. We note that under a *DC* bias, the diffusion boundary layer is polarized [18]. The ionic concentration decreases from the bulk to the interface in the depletion microchannel and increases near the enrichment microchannel interface. The enrichment effects do not significantly contribute to the DBL resistance [23]. However, the decrease in the concentration near the depletion interface increases the diffusional DBL resistance. Hence, we observe a slight increase in the impedance of the diffusional arc. Also for the applied *DC* bias, we observe negligible change in the electric migration process inside the microchannel and nanochannel, compared to the no bias case. Hence, the distorted geometric arc overlaps with the previous no bias case. The resistance due to the electromigration process in both the microchannels and the nanochannel can be estimated from the width of the geometric arc. The total width of the impedance spectrum gives the total

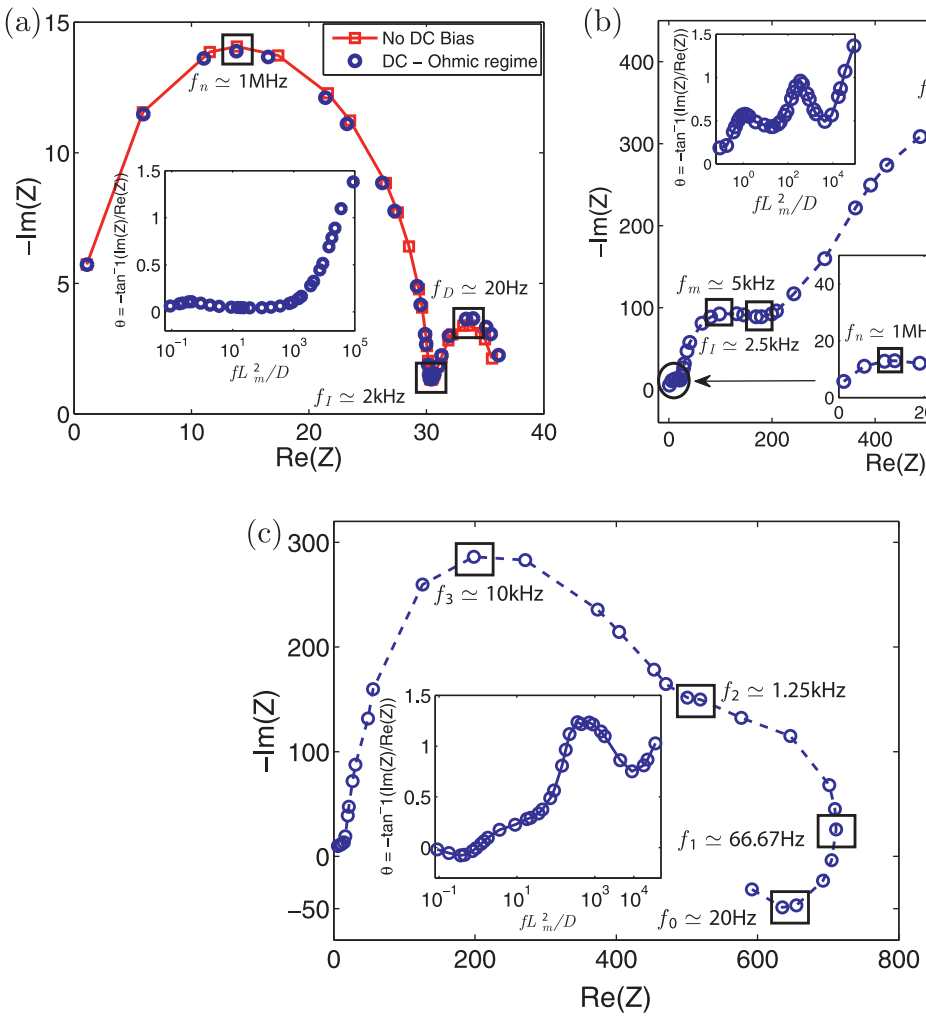

Fig. 4. (a) Comparison of impedance spectra between no external *DC* bias (line with symbol) and *DC* bias ($\phi_{DC}Fz/RT = 3.8684$), corresponding to Ohmic regime (circles). The inset of the figure shows Bode phase plot under Ohmic regime. (b) Impedance spectrum at $\phi_{DC}Fz/RT = 77.3677$, corresponding to limiting resistance regime. The insets of the figure show the Bode phase plot and the high frequency arc corresponding to the nanochannel transport. (c) Impedance spectrum at $\phi_{DC}Fz/RT = 773.677$, corresponding to overlimiting regime. The inset of figure shows Bode plot to illustrate phase effects. In all these cases, $\beta = 5.1334 \times 10^{-3}$.

resistance of the system, under *DC* bias. In spite of the presence of depletion and enrichment DBL regions, electroneutrality is maintained in the microchannel (beyond the EDL interface). Hence, the length of the DBL region is unaffected in the Ohmic regime, resulting in the same characteristic diffusion frequency (f_D). The inset of the figure displays the Bode plot indicating the relative phase difference ($\theta = -\tan^{-1}(Im(Z)/Re(Z))$) with respect to different normalized frequency. We observe a phase shift maximum corresponding to the characteristic diffusional frequency, f_D. A monotonic increase in the phase at frequencies greater than f_I is attributed to the capacitive effects of the microchannel and nanochannel rather than that of the EDL.

A further increase in the *DC* bias, $\phi_{DC}Fz/RT = 77.3677$ corresponding to the limiting resistance regime, results in the breakdown of the classical diffusional arc and the merging of the two characteristic arcs as shown in Fig. 4(b). The merging is accompanied by an additional resistance–capacitance (RC) arc with a new characteristic frequency, f_m. We also observe an increase in the frequency, f_D. We attribute these effects to the space charges induced due to the strong electromigration effects near the micro–nanochannel depletion junction. To confirm this physics, we numerically calculate the total charge (Q_{SCR}) per unit width in the induced space charge region (SCR), by integrating the space charge density ($\hat{\rho}_e = Fz(\hat{c}_+ - \hat{c}_-)$), along the length of SCR. We also assume that the charges predominantly propagate toward the microchannel in the LRR regime. The charge propagation reduces the length of the electroneutral depletion DBL. Substituting the new diffusional frequency (f_D) in the expression for f_D, we obtain the reduced DBL length (L_{DBL}^{new}) and the corresponding length of the SCR, $L_{SCR} = L_m - L_{DBL}^{new}$. The total charge per unit width is $Q_{SCR} = 2H_m \int_{x_e}^{L_{SCR}} \hat{\rho}_e \, dx$. x_e is the coordinate where the nanochannel ends. We determine the capacitance inside the SCR (C_{SCR}) by calculating the corresponding voltage drop ($V_{SCR} = \hat{\phi}|_{L_{SCR}} - \hat{\phi}|_{x_e}$); $C_{SCR} = Q_{SCR}/V_{SCR}$. Knowing the total current per unit width (I), the new characteristic frequency in the SCR is calculated as $f_m = 1/2\pi R_{SCR} C_{SCR}$. Here $R_{SCR} = V_{SCR}/I$. Substituting all the numerical values [$L_{DBL}^{new} = 4.925\,\mu m$, $L_{SCR} = 1.0705\,\mu m$, $Q_{SCR} = 0.2656\,nC/m$, $V_{SCR} = 0.3163\,V$, $I = 8.6332\,\mu A/m$, $C_{SCR} = 0.8396\,nF/m$, $R_{SCR} = 36.643\,k\Omega m$], the approximate characteristic frequency is 5.1735 kHz which is in good agreement with the numerical simulation, and hence, confirming our hypothesis. The above analysis also helps us to understand that the impedance spectra can be used to measure the reduced microscopic DBL and new SCR lengths in the LRR regime without probing inside the microchannel. This is unlike the earlier probing techniques [23,38], in which the thickness of the vortex array, developed due to the instabilities in the space charge region is measured to characterize the same. The inset of

the figure displays the Bode phase plot where we observe a second phase-shift maximum at a characteristic frequency, $fL_m^2/D = 360$, unlike the previous case. Similar characteristics are also observed for a higher *DC* bias ($\phi_{DC}Fz/RT = 154.735$), corresponding to the LRR regime. This feature is observed even without considering the displacement current (see Fig. (S3) in the supporting information) which illustrates that it is due to the strong electrophoretic interaction resulting in the induced space charges near the depletion interface. Finally, the third arc with characteristic frequency f_n, along with an increase in the phase (θ) at $f \geq f_n$ (as shown in the Bode phase plot in the inset of Fig. 4(b)) reveal the electric migration and capacitance effects of the nanochannel.

We now repeat the analysis, in the third regime at a *DC* bias ($\phi_{DC}Fz/RT = 773.677$), corresponding to the overlimiting behavior, which results in a higher current in the *I–V* characteristics (see Fig. (S1)). The overlimiting regime in a negatively charged nanochannel was characterized owing to the redistribution of the charges near the micro–nanochannel depletion interface [17]. This redistribution is accompanied by an enhanced conductivity of the chloride ions near this interface, resulting in an enhanced current. Fig. 4(c) shows the impedance spectrum in this regime. We observe an anomalous inductive arc at low frequencies, $fL_m^2/D \leq 1$, which is revealed by the change in the sign of the imaginary part of the impedance. In other words, at these frequencies, the applied electric potential leads the output current ($\theta_I - \theta_V < 0$) as shown by the Bode phase plot in the inset of Fig. 4(c). As the harmonic electric potential disturbance is applied at a constant phase angle ($\theta_V = 3\pi/2$), the changes in the phase of the output current should result in the inductive behavior. In order to understand these changes, we calculate the electric migration current per unit width in the induced space charge region using Eq. (4). Under the application of combined *AC* and *DC* electric potential, we assume, $(\hat{c}_+ + \hat{c}_-) = C_0 + C_1\, cos(\omega t + \theta_1)$ and $\frac{d\hat{\phi}}{dx} = \phi_{x_0} + \phi_{x_1}\, cos(\omega t + \phi_1)$, neglecting the contribution of other higher harmonic components. C_0, ϕ_{x_0} are the *DC* component of the total ionic concentration and the field, respectively. C_1, ϕ_{x_1} are the respective first harmonic contributions of the ionic concentration and field. θ_1 and ϕ_1 are the corresponding phase angles of the former and latter terms, respectively. Substituting the aforementioned expressions into Eq. (4) and multiplying the resulting current by -1 to be consistent with the output current obtained from the numerical simulations (see supporting information), the current per unit width due to the combined *AC* and *DC* bias is calculated as,

$$I(t) = \frac{2F^2z^2DH_m}{RT}[C_0\phi_{x_0} + (C_0\phi_{x_1}cos\phi_1 + C_1\phi_{x_0}cos\theta_1)cos\omega t - (C_0\phi_{x_1}sin\phi_1 + C_1\phi_{x_0}sin\theta_1)sin\omega t] \quad (5)$$

Here we also assume $C_1\phi_{x_1} \ll C_0\phi_{x_0}$. Comparing Eq. (5) and Eq. (2), we obtain the phase angle of the output current, $\theta_I = \tan^{-1}(b_1/a_1)$, where $a_1 = [(2F^2z^2DH_m)/(RT)][(C_0\phi_{x_1}cos\phi_1 + C_1\phi_{x_0}cos\theta_1)]$ is the real part and $b_1 = [(2F^2z^2DH_m)/(RT)][(C_0\phi_{x_1}sin\phi_1 + C_1\phi_{x_0}sin\theta_1)]$ is the imaginary part of the harmonic output current per unit width.

All the above variables are numerically calculated in the induced space charge region at $x/L_m = 1.9167$, for a given *DC* bias of $\phi^{DC}Fz/RT = 773.677$ and $\phi^{DC}Fz/RT = 77.3677$. The values corresponding to overlimiting regime are tabulated in Table S1 (see supporting information) while that corresponding to the LRR is shown in Table S2 (see supporting information). From Table S1, we observe that in the overlimiting regime, the total ionic concentration and field tend to be in-phase with each other (i.e., $(|\theta_1 - \phi_1| < \pi/2)$. Also, at low frequencies, $fL_m^2/D \leq 1$, the phase of the ionic concentration is less than $3\pi/2$, while that of the field is greater than $3\pi/2$. As the perturbed concentration marginally lags behind the field, we observe that the real part of the harmonic current becomes less than zero ($a_1 < 0$), along with the imaginary component, $b_1 < 0$. As both the real and imaginary part of the current are negative the phase angle of the output current is in the third quadrant, i.e., $\pi \leq \theta_I \leq 3\pi/2$. This implies that the output current is lagging behind the applied perturbed voltage (as $\theta_V = 3\pi/2$), resulting in the inductive behavior. Further, we observe a maximum lag between the output current and applied voltage when there is a maximum lag between the perturbed concentration and the electric field. This occurs at $fL_m^2/D = 0.36$, corresponding to a dimensional frequency of $f_0 = 20$ Hz. At higher frequencies, $fL_m^2/D > 1$, the perturbed concentration leads the field ($\theta_1 > \phi_1 > 3\pi/2$) which results in a positive contribution in a_1, while b_1 is still negative. Hence, the phase angle of the current is in the fourth quadrant, implying that the current leads the applied voltage. Thus, at high frequencies we observe capacitive arc in the impedance spectrum. These arguments also help us to conclude that the origin of the inductive arc is due to the migration of the charges near the induced space charge region, as we have neglected the diffusive and displacement currents in the analysis. Additional computations were performed for another *DC* voltage ($\phi_{DC}Fz/RT = 580.258$) corresponding to the overlimiting regime to ensure consistency in the observation.

We repeated our analysis in the LRR regime under similar range of harmonic excitations. Table S2 (see supporting information) shows that even though the harmonic concentration lags behind the field, they are always out of phase with each other by more than π. Under these conditions, a_1 and b_1 was always found to be in the fourth quadrant. These effects result in the current leading the applied voltage at all the frequencies, and hence, we observe only capacitive type behavior. Fig. 4(c) also shows that the inductive arc is accompanied by three deformed hemicircle arcs. The width of the impedance spectrum in the second arc (above the inductive arc) is lower compared to the limiting resistance regime. The increased chloride ion conductivity near the micro–nanochannel depletion junction is attributed to this lower impedance. We also observe an increase in the width of the third arc compared to the LRR regime with a new characteristic frequency, $f_3 = 10$ kHz. We attribute these results to the fact that with increase in the *DC* bias, the length of the space charge region near the depletion interface increases resulting in a higher voltage drop and charge density. We would like to point out that in the entire impedance analysis, the amplitude of the harmonic disturbance is ensured to be small so that they do not interfere with the impedance spectra. This was checked by performing additional simulations with different small *AC* amplitude. The results are included in the supporting information, in Fig. S4. We also extend our study and probe the limiting resistance regime, with the magnitude of *AC* perturbation comparable to the *DC* bias. The results are discussed in the supporting information. We highlight that the small amplitude CIS technique can be used to predict the important time scales at which different *AC* current rectification characteristics are observed.

4.3. Equivalent circuit model design

Under no external *DC* bias, considering all the five regions inside the integrated micro–nanochannel independently, we can understand the transport in each region using the following circuit elements. A finite length diffusion element (Z_D^s) in parallel with an EDL capacitor (C_{EDL}^s) is used to represent the diffusion-transport in the DBL, and the EDL charging effects. The superscript "s" indicates the source microchannel. To understand the electric migration process and the capacitance effects in the source microchannel, a resistor, R_m^s in parallel with a capacitor, C_m^s is considered. The aforementioned circuit elements are also used to model the transport in the drain microchannel, which are distinguished from the former elements with a superscript "D". Finally, the migration process and

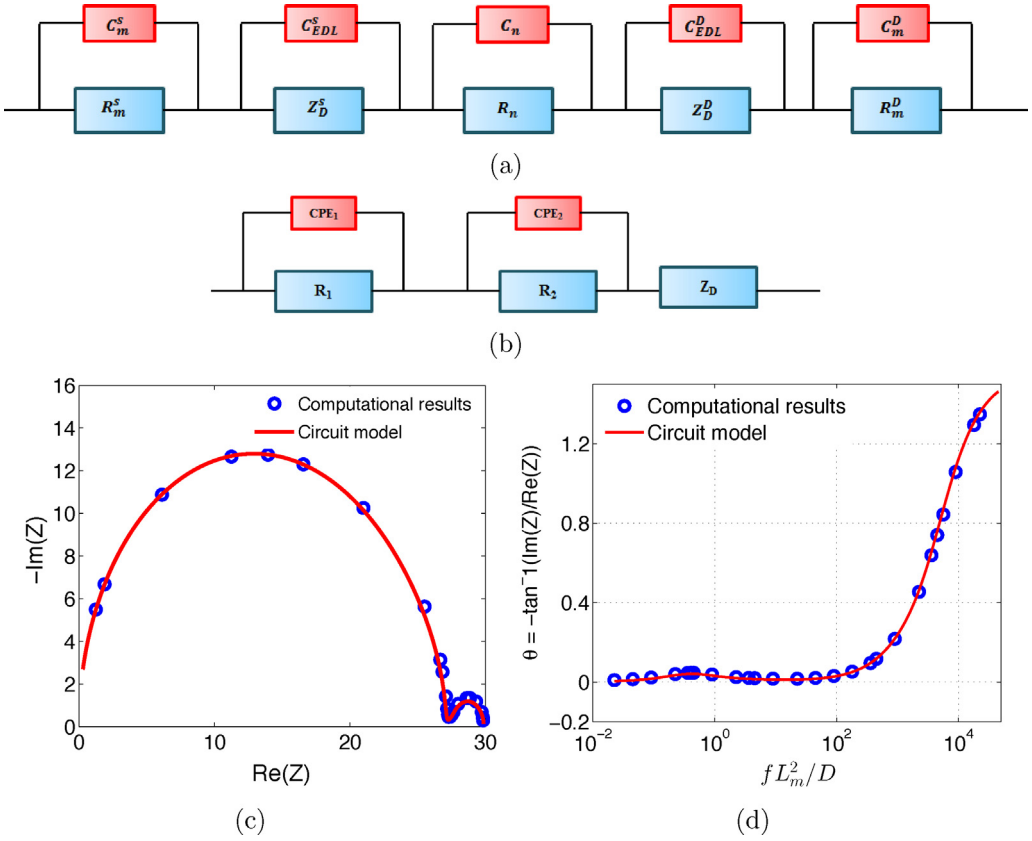

Fig. 5. (a) A physically consistent equivalent circuit model. (b) Modified circuit model. Comparison of (c) computational impedance spectra, (circles) and (d) Bode phase plot results, (circles) with the equivalent circuit model (solid line) under no external *DC* bias at $\beta = 5.1334 \times 10^{-3}$, and $L_m = 3$ μm.

the displacement effects inside the nanochannel can be characterized using a resistor, R_n in parallel with a capacitor, C_n. Fig. 5(a) shows a series representation of the discussed circuit elements to represent the *AC* impedance response of MNECS. Owing to the presence of multiple EDLs at the micro–nanochannel interface, it is almost impossible to determine the individual capacitance and also the impedance Z_D analytically. Also, it is difficult to fit them as there are many unknown parameters. Hence, we propose a modified equivalent circuit in which the migration and displacement effects in the nanochannel and microchannel are characterized using a resistor in parallel with a constant phase element (CPE) [24]. A CPE is used instead of an ideal capacitor, with an arbitrary factor n owing to the non-ideal behavior arising due to the EDL effects. We note that n can vary from −1 to 1, where the end values illustrate an ideal inductor and a capacitor, respectively. Further, we characterize the migration effects in both the microchannels using a single R||CPE element. A single finite length diffusion element, whose functional form is given by Eq. (3) is used to characterize the diffusion-transport in both the DBLs. Fig. 5(b) shows the modified equivalent circuit. Considering these elements in series, the functional form to characterize the impedance spectra under no external *DC* bias is represented as,

$$Z(\omega) = \left(\frac{1}{R_1} + (j\omega)^{n_1} CPE_1\right)^{-1} + \left(\frac{1}{R_2} + (j\omega)^{n_2} CPE_2\right)^{-1} + R_D \frac{tanh[\sqrt{(j\omega\tau_D)}]}{\sqrt{(j\omega\tau_D)}} \quad (6)$$

where R_1, CPE_1 represent the resistance, constant phase element of the nanochannel, respectively. R_2, CPE_2 represent the resistance, constant phase element of both the microchannels, respectively. n_1, n_2 are the arbitrary factors. To determine R_1, CPE_1, and n_1, we neglect the microchannel and perform the simulations considering only a nanochannel of length $L_n = 5$ μm and $H_n = 15$ nm at a constant $\beta = 5.1334 \times 10^{-3}$. A perfect hemicircle with a single characteristic frequency is observed in the impedance spectrum. The data is fitted to Eq. (6) (considering only the first term) using non-linear least squares method. The obtained values are tabulated in Table 2. Using these values, we characterize the impedance response for the entire micro–nanochannel integrated system, with the microchannel length $L_m = 3$ μm and $H_m = 500$ nm. R_D is obtained by measuring the width of the diffusional arc, while, R_2, CPE_2 and n_2 are obtained by fitting the overall impedance spectrum. All the values are tabulated in Table 2. The values are substituted in Eq. (6) and is normalized with $(RT/F^2z^2Dc_0)$. A comparison between the computational results (shown as circles) and the equivalent circuit model (shown as solid line) give fairly good agreement with each other as shown by the Nyquist plot (see Fig. 5(c)) and the Bode phase plot

Table 2
Fitting parameters for the circuit model under no external *DC* bias and under limiting resistance regime.

Parameters	No *DC*	$\phi_{DC}Fz/RT = 77.3677$
R_1 (kΩm)	32.429	27
R_2 (kΩm)	3.8	175
R_3 (kΩm)	NA	120
CPE_1	4.482e−12	5.8086e−12
CPE_2	2.3611e−10	1.6e−10
CPE_3	NA	14e−9
n_1	1	1
n_2	0.97	1
n_3	NA	1
R_D (kΩm)	3.8	940
τ_D (ms)	4.5	12.1

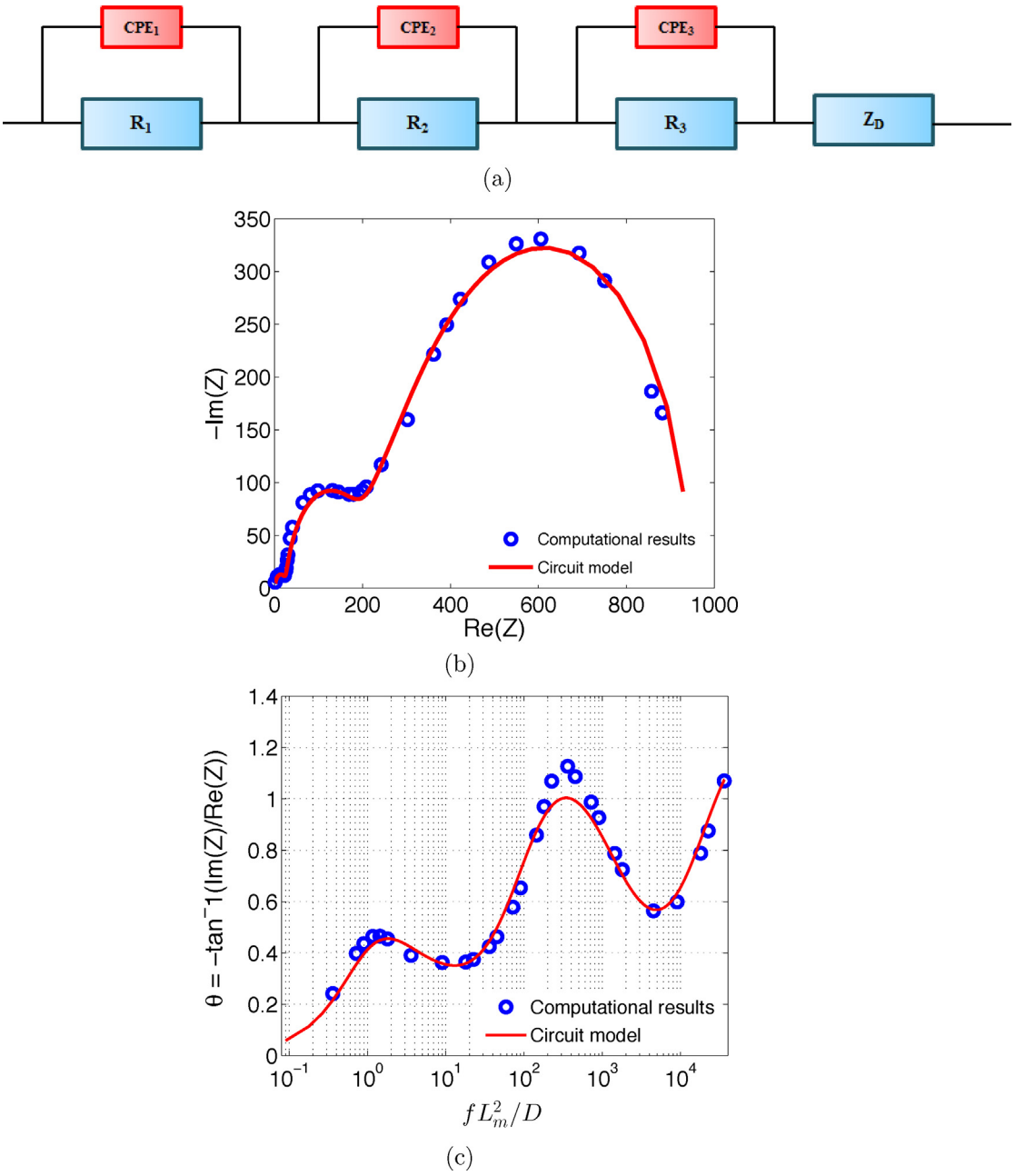

Fig. 6. (a) An equivalent circuit model. Comparison of (b) computational impedance spectra, (circles) and (c) Bode phase plot results, (circles) with the equivalent circuit model (solid line) under limiting resistance regime ($\phi_{DC}Fz/RT = 77.3677$) at $\beta = 5.1334 \times 10^{-3}$, and $L_m = 6$ μm.

(see Fig. 5(d)). Also, the same functional form provides reasonably good match in the Ohmic regime.

In the limiting resistance regime, owing to the presence of induced space charges the model fails to predict an additional resistance–capacitance arc. To overcome this, we considered an additional (R‖CPE) circuit element in series with the previous model as shown in Fig. 6(a) for a *DC* bias, $\phi_{DC}Fz/RT = 77.3677$. The new circuit model provides a reasonable agreement with the computational simulations as shown in Fig. 6(b). Furthermore, the multiple phase shift maximum at different frequencies is qualitatively captured as shown in Fig. 6(c). The relevant parameters used in the model are tabulated in Table 2. An accurate agreement with the computational results can be obtained by a systematic parameterization of the circuit elements. Using the same model, we observed a good agreement with the computational results for a higher *DC* voltage, $\phi_{DC}Fz/RT = 154.735$, corresponding to the LRR regime. An equivalent circuit to characterize the complex overlimiting behavior is beyond the scope of the present work. We would also like to mention that, though the AAM model is developed to understand the ion transport dynamics for a nanochannel of uniform geometry and with homogeneous charge distribution, it could potentially be extended to investigate asymmetric channels like conical nanopores. Owing to the inherent loss of symmetry, one can achieve rectification effects and control the ionic transport under *AC* bias even in the absence of *DC* field. This provides a promising step toward slowing down DNA translocation across nanopores and also helps us to characterize them effectively, which is currently the need of the hour for DNA sequencing.

5. Conclusions

To summarize, a computational impedance spectroscopic technique (CIS) is developed to characterize the fundamental electrochemical properties of a micro–nanochannel integrated system using an area-averaged multi-ion transport model. The technique is used to investigate the ion transport dynamics with and without the influence of external *DC* bias. Under no external *DC* bias and in the Ohmic regime, we observed two distinct arcs with four different characteristic frequencies. The low frequency diffusional arc characterizes the diffusion-transport and the EDL charging effects at the interface of the micro–nanochannel, while the high frequency geometric arc characterizes the electric migration and displacement current effects inside the microchannel and in the nanochannel. An additional resistance–capacitance (RC) arc with a new characteristic frequency f_m is observed in the LRR regime. The presence of induced space charges in the depletion microchannel was attributed to these effects. Further, an anomalous inductive arc at low frequencies ($fL_m^2/D \leq 1$) was observed in the overlimiting regime. The origin of this arc was attributed to the phase effects between the harmonic disturbance of the total ionic concentration and the electric field in the induced space charge region. The presence of an anomalous inductive arc provides an opportunity to distinguish the LRR and overlimiting region. Furthermore, in the Ohmic and in the LRR regimes, the impedance spectra helps us to characterize the microscopic length of the diffusion boundary layer (DBL) and the space charge region (SCR). Using the impedance spectra, we also highlight the important time scales at which negative and positive *AC* rectification effects are observed in the system. Finally, equivalent circuit models are designed to interpret the impedance response.

Acknowledgements

This work was supported by the National Science Foundation (NSF) under Grants 0328162 (nano-CEMMS, UIUC), 0852657, 0915718 and 0941497. The authors gratefully acknowledge the use of the parallel computing resource provided by the University of Illinois. V.N. thanks Micheal Campbell for fruitful discussions and help with regard to efficient resource utilization in the parallel cluster.

Appendix A. Supplementary data

Supplementary data associated with this article can be found, in the online version, at http://dx.doi.org/10.1016/j.electacta.2013.05.011.

References

[1] C. Dekker, Solid-state nanopores, Nature Nanotechnology 2 (2007) 209.
[2] M. Krems, Y.V. Pershin, M.D. Ventra, Ionic memcapacitive effects in nanopores, Nano Letters 10 (2010) 2674.
[3] Z. Siwy, A. Fulinski, Fabricaiton of a synthetic nanopore ion pump, Physical Review Letters 89 (2002) 198103.
[4] M.J. Vitarelli Jr., S. Prakash, D.S. Talaga, Determining nanocapillary geometry from electrochemical impedance spectroscopy using a variable topology network circuit model, Analytical Chemistry 83 (2011) 533.
[5] R.B. Schoch, J. Han, P. Renaud, Transport phenomena in nanofluidics, Reviews of Modern Physics 80 (2008) 839.
[6] S. Howorka, Z. Siwy, Nanopore analytics: sensing of single molecules, Chemical Society Reviews 38 (2009) 2360.
[7] O.A. Saleh, L.L. Sohn, An artificial nanopore for molecular sensing, Nano Letters 3 (2003) 37.
[8] Z. Chen, Y. Jiang, D.R. Dunphy, D.P. Adams, C.H.N. Liu, N. Zhang, G. Xomeritakis, X. Jin, N.R. Aluru, S.J. Gaik, H.W. Hillhouse, C.J. Brinker, DNA translocation through an array of kinked nanopores, Nature Materials 9 (2010) 667.
[9] J.J. Kasianowicz, E. Brandin, D. Branton, D.W. Deamer, Characterization of individual polynucleotide molecules using a membrane channel, Proceedings of the National Academy of Sciences of the United States of America 93 (1996) 13770.
[10] H. Chang, F. Kosari, G. Andreadakis, M.A. Alam, G. Vasmatzis, R. Bashir, DNA-mediated fluctuations in ionic current through silicon oxide nanopore channels, Nano Letters 4 (2004) 1551.
[11] J.B. Heng, C. Ho, T. Kim, R. Timp, A. Aksimentiev, Y.V. Grinkova, S. Sligar, K. Schulten, G. Timp, Sizing DNA using a nanometer-diameter pore, Biophysical Journal 87 (2004) 2905.
[12] A. Piruska, M. Gong, J.V. Sweedler, P.W. Bohn, Nanofluidics in chemical analysis, Chemical Society Reviews 39 (2010) 1060.
[13] S.J. Kim, S.H. Ko, K.H. Kang, J. Han, Direct seawater desalination by ion concentration polarization, Nature Nanotechnology 5 (2010) 297.
[14] X. Jin, S. Joseph, E.N. Gatimu, P.W. Bohn, N.R. Aluru, Induced electrokinetic transport in micro–nanofluidic interconnect devices, Langmuir 23 (2007) 13209.
[15] T. Postler, Z. Slouka, M. Svoboda, M. Přibyl, D. Šnita, Parametrical studies of electroosmotic tranport characteristics in submicrometer channels, Journal of Colloid and Interface Science 320 (2008) 321.
[16] Y.S. Choi, S.J. Kim, Electrokinetic flow-induced currents in silica nanofluidic channels, Journal of Colloid and Interface Science 333 (2009) 672.
[17] V.V.R. Nandigana, N.R. Aluru, Understanding anomalous current–voltage characteristics in microchannel-nanochannel interconnect devices, Journal of Colloid and Interface Science 384 (2012) 162.
[18] Q. Pu, J. Yun, H. Temkin, S. Liu, Ion-enrichment and ion-depletion effect of nanochannel structures, Nano Letters 4 (2004) 1099.
[19] A. Mani, T.A. Zangle, J.G. Santiago, On the propagation of concentration polarization from microchannel–nanochannel interfaces. Part I. Analytical model and characteristic analysis, Langmuir 25 (2009) 3898.
[20] T.A. Zangle, A. Mani, J.G. Santiago, On the propagation of concentration polarization from microchannel–nanochannel interfaces. Part II. Numerical and experimental study, Langmuir 25 (2009) 3909.
[21] S.J. Kim, Y.-C. Wang, J.H. Lee, H. Jang, J. Han, Concentration polarization and nonlinear electrokinetic flow near a nanofluidic channel, Physical Review Letters 99 (2007) 044501.
[22] G. Yossifon, H.-C. Chang, Selection of non-equilibrium over-limiting currents: universal depletion layer formation dynamics and vortex instability, Physical Review Letters 101 (2008) 254501.
[23] G. Yossifon, P. Mushenheim, Y.C. Chang, H.-C. Chang, Nonlinear current–voltage characteristics of nano-channels, Physical Reviews E 79 (2009) 046305.
[24] E. Barsoukov, J.R. Macdonald, Impedance Spectroscopy: Theory, Experiment and Applications, 2nd ed., Wiley, Hoboken, NJ, 2005.
[25] J. Feng, J. Liu, B. Wu, G. Wang, Impedance characteristics of amine modified single glass nanopores, Analytical Chemistry 82 (2010) 4520.
[26] E.N. Ervin, H.S. White, L.A. Baker, Alternating current impedance imaging of membrane pores using scanning electrochemical microscopy, Analytical Chemistry 77 (2005) 5564.
[27] V.V. Nikonenko, A.E. Kozmai, Electrical equivalent circuit of an ion-exchange membrane system, Electrochimica Acta 56 (2011) 1262.
[28] A.A. Moya, Influence of dc electric current on the electrochemical impedance of ion-exchange membrane systems, Electrochimica Acta 56 (2011) 3015.
[29] A.A. Moya, Electric circuits modelling the low-frequency impedance of ideal ion-exchange membrane systems, Electrochimica Acta 62 (2011) 296.
[30] A.A. Moya, Harmonic analysis in ideal ion-exchange membrane systems, Electrochimica Acta 90 (2013) 1.
[31] http://www.openfoam.com/, 2011.
[32] M. Frigo, S.G. Johnson, Fftw: an adaptive software architecture for the fft, Proceedings of the International Conference on Acoustics, Speech, and Signal Processing 3 (1998) 1381.
[33] B. Hille, Ion Channels of Excitable Membranes, 3rd ed., Sinauer Associates Inc., Sunderland, MA, 2001.
[34] I. Rubinstein, B. Zaltzman, A. Futerman, V. Gitis, V. Nikonenko, Reexamination of electrodiffusion time scales, Physical Reviews E 79 (2009) 021506.
[35] I. Rubinstein, B. Zaltzman, Probing the extended space charge by harmonic disturbances, Physical Reviews E 80 (2009) 021505.
[36] T. Jacobsen, K. West, Diffusion impedance for planar, cylindrical, and spherical geometry, Electrochimica Acta 40 (1995) 255.
[37] J.P. Diard, B.L. Gorrec, C. Montella, Linear diffusion impedance. General expression and applications, Journal of Electroanalytical Chemistry 471 (1999) 126.
[38] I. Rubinstein, E. Staude, O. Kedem, Role of the membrane surface in concentration polarization at ion-exchange membrane, Desalination 69 (1988) 101.